

# XAFS Studies of Surface Structures of TiO<sub>2</sub> Nanoparticles and Photocatalytic Reduction of Metal Ions

Lin X. Chen,\* Tijana Rajh, Zhiyu Wang, and Marion C. Thurnauer

Chemistry Division, Argonne National Laboratory, 9700 South Cass Avenue, Argonne, Illinois 60439

Received: June 13, 1997; In Final Form: September 26, 1997<sup>®</sup>

To probe the origin of the unique functions of titanium dioxide (TiO<sub>2</sub>) nanoparticles observed in photocatalytic reactions, structures of Ti atom sites in titanium dioxide (TiO<sub>2</sub>) nanoparticles with different sizes were studied by Ti K-edge XAFS (X-ray absorption fine structure). Compared to the bulk TiO<sub>2</sub> structure, a shorter Ti–O distance from surface TiO<sub>2</sub> resulting from Ti–OH bonding was observed. The XAFS spectra also revealed an increasing disorder of the lattice with decreasing sizes of the nanoparticles based on a coordination number decrease for the third-shell O atoms as well as changes in relative intensities of preedge peaks A<sub>1</sub>, A<sub>2</sub>, and A<sub>3</sub>. However, the Ti sites largely remain octahedral even in the 30 Å diameter particles. These results imply that the increasing number of surface Ti sites as well as possible corner defects in small nanoparticles may be the main cause of the unique surface chemistry exhibited by nanoparticles of TiO<sub>2</sub>. XAFS was also used in monitoring the photoreduction reaction products of Cu<sup>2+</sup> and Hg<sup>2+</sup> on TiO<sub>2</sub> nanoparticle surfaces, with or without surface adsorbers, alanine (Ala) and thiolactic acid (TLA). Ala dramatically enhanced photoreduction of Cu<sup>2+</sup> on TiO<sub>2</sub> nanoparticle surfaces, whereas thiolactic acid did not affect or even hindered Hg<sup>2+</sup> photoreduction. Although both surface adsorbers chelated with the metal ions in the absence of TiO<sub>2</sub> nanoparticles, this chelation was drastically changed in the Cu–Ala complex but was largely retained in the Hg–TLA complex when TiO<sub>2</sub> was present. This may correlate with the different effects of the adsorbers on the photoreduction of the metal. Our experimental results suggest that a proper balance between the affinities of the adsorber to the metal ions and to the surface Ti atoms of TiO<sub>2</sub> may be one of the keys in selecting a surface adsorber for enhanced photoreduction efficiency.

## I. Introduction

Photocatalytic reactions on TiO<sub>2</sub> surfaces are very important in environmental cleanup and remediation,<sup>1–6</sup> such as oxidation of organic material and reduction of heavy metal ions in industrial waste streams.<sup>7–11</sup> Differing from the bulk material, TiO<sub>2</sub> nanoparticles are expected to have unique surface chemistry due to their larger surface area.<sup>12</sup> Photoirradiation of TiO<sub>2</sub> nanoparticles, with photon energies larger than the bandgap (3.2 eV), creates electron–hole (e<sup>−</sup>/h<sup>+</sup>) pairs,



Consequently, following irradiation, the TiO<sub>2</sub> nanoparticles act as either electron or hole donors to reduce or oxidize materials in the surrounding media. However, the photoinduced charge separation in bare TiO<sub>2</sub> nanoparticles has a very short lifetime because of charge recombination. Therefore, it is important to prevent the hole–electron recombination before a designated redox reaction occurs. One way to accomplish this is to scavenge photogenerated holes or electrons with molecules strongly adsorbed onto TiO<sub>2</sub> surfaces.<sup>11,13</sup> In this way, scavenged charge carriers can be transported away from the surface of the TiO<sub>2</sub> particles, providing a larger spatial separation between the photogenerated holes and electrons. Consequently, the lifetime of charge separation is prolonged, and the photocatalytic activity of TiO<sub>2</sub> particles may be increased. Recent EPR studies indicated enhanced redox activities of surface-modified TiO<sub>2</sub> particles as a result of transferring the photogenerated holes away from the TiO<sub>2</sub> surface through the surface adsorbed molecules.<sup>11</sup>

Although many observations led to the same conclusions that photocatalytic activities were higher in TiO<sub>2</sub> nanoparticles compared to the bulk and sometimes higher in modified nanoparticles compared to the bare particles, the mechanisms for the enhancement were not completely clear. To further our understanding of the reaction mechanisms, we examine in this work (1) the surface and lattice structures of TiO<sub>2</sub> nanoparticles and (2) oxidation states of the metal photoreduction products. In previous work, metallic states were identified from the optical absorption spectra that had an onset of absorption below 800 nm. However, these spectra can also be characteristic of binary semiconductors with small bandgaps. Thus, positive identification of the metal oxidation states following photoinduced reaction is crucial to understanding the reaction mechanisms.

The techniques of X-ray absorption spectroscopy (XAS), namely X-ray absorption near edge structure (XANES) and X-ray absorption fine structure (XAFS), probe local structural details around specific metal atoms and are sensitive to the oxidation states of the metal.<sup>14</sup> At the Ti K-edge, structural changes around Ti atoms as a function of the particle sizes can be probed, and this could be correlated with the unique surface reactivities of TiO<sub>2</sub> nanoparticles. At the metal absorption edges (K or L), XAFS can be used to examine the surroundings of the metal species adsorbed on the TiO<sub>2</sub> nanoparticle. Comparison of spectra from TiO<sub>2</sub> nanoparticles with and without surface-adsorbed small molecules as obtained with and without photoillumination provides evidence for metal photoreduction and interactions between metal ions and TiO<sub>2</sub> surface or adsorbed species. Correlations between the structures of the metal complexes and their photoreduction reactivities can be established through such studies. This correlation, if any, will help in the selection of TiO<sub>2</sub> nanoparticle surface modifiers that will enhance reaction efficiencies.

\* To whom correspondence should be addressed: FAX (630) 252-9289, e-mail lchen@anlchm.chm.anl.gov.

<sup>®</sup> Abstract published in *Advance ACS Abstracts*, November 15, 1997.

In this paper, we use XAFS to investigate the effect of the size on the lattice structure of TiO<sub>2</sub> nanoparticles. In the size regime of nanoparticles (e.g., particles with diameters of 20–100 Å), a significant fraction of the atoms are located on the surface (e.g., ~40% for 30 Å diameter TiO<sub>2</sub> particles; see below). Therefore, it is feasible to probe by XAFS the unique structural features around surface Ti atoms in TiO<sub>2</sub> nanoparticles. Both structures for the interior and surface TiO<sub>2</sub> can be characterized by comparing the XAFS spectra of TiO<sub>2</sub> particles of different sizes. In addition, we also used XAFS to monitor metal ion photoreduction of Cu<sup>2+</sup> and Hg<sup>2+</sup> on TiO<sub>2</sub> colloid surfaces with and without surface modifiers. The oxidation state of the metal ions in these processes can be identified directly by XANES at respective metal absorption edges. The correlation of the reaction efficiency and the structures of the metal complexes with TiO<sub>2</sub> or surface adsorbers will be discussed.

## II. Experimental Section

**1. Sample Preparation.** All chemicals were reagent grade from Aldrich or Baker Chemical Companies and used without further purification. The TiO<sub>2</sub> particles with 30, 50, and 200 Å diameters were prepared by dropwise addition of titanium(IV) chloride to cooled water. The details of preparation are presented elsewhere.<sup>15</sup> The TiO<sub>2</sub> nanoparticles with 400 Å diameters were gifts from Nanophase Inc. The sizes of the colloid particles were determined by electron microscopy. Ala or TLA/metal ion mixtures were made with concentrations of 0.02 M/0.01 M, respectively. The metal ion concentration in all starting solution samples was 0.01 M. Methanol was added as a hole scavenger to all TiO<sub>2</sub>-containing samples with mercury ions and without surface adsorber. Copper and mercury acetate salts were dissolved in aqueous solutions as respective metal ion sources.

The photoillumination was provided by an ILC UV-enhanced xenon lamp (150 W). The sample with a mixture of TiO<sub>2</sub> nanoparticles and metal ion solution (0.01 M) was sealed in an airtight glass cell and stirred constantly during the illumination. The sample container was placed in a continuous flow water bath with a glass wall to maintain the sample at constant temperature during irradiation. After a certain time of illumination the sample was put into a bag which had a continuous nitrogen gas flow. An aliquot of the mixture was filtered and transferred under nitrogen atmosphere from the glass cell to a sealed XAFS cell for the measurement. The remaining mixture was kept in the dark under nitrogen atmosphere until the next illumination. This procedure was repeated for samples with different illumination times. The illumination time was the total time that the sample was exposed to the lamp.

**2. XAFS Measurements.** XAFS experiments were carried out at Beamlines X6B, X18B, and X19A of the National Synchrotron Light Source (NSLS) at Brookhaven National Laboratory. In Beamlines X6B and X19A, the X-ray beam was focused, and the spot size at the sample was 1 mm × 0.5 mm. In X18B, the beam size at the sample was 15 mm × 1 mm. A Si(111) double-crystal monochromator was used for Ti K-edge (4.966 keV) experiments, and a Si(220) monochromator crystal was used for metal K- or L-edge experiments. The monochromator was detuned by 20–50% in order to reduce the harmonic component in the incident X-ray at the sample. The scans were collected from –100 to 1000 eV relative to the transition edge energies which were calibrated using TiO<sub>2</sub> powder and metal foils.

For TiO<sub>2</sub> and reference compound powder samples, the transmission detection by ion chambers (helium gas for Ti K-edge, nitrogen gas for Cu K-edge and Hg L<sub>III</sub>-edge) was used.

For filtered TiO<sub>2</sub> gel samples with metal ions, X-ray fluorescence detection was carried out using a Lytle detector with a proper filter. No filter was used for measurements at the Ti K-edge. A nickel or germanium filter was used for the measurements at the Cu K-edge or the Hg L<sub>III</sub>-edge, respectively. At the Ti K-edge, helium gas was used to purge the sample chamber of the Lytle detector. For most of the solid TiO<sub>2</sub> nanoparticle and reference compound powders, the sample was sandwiched between two pieces of Kapton tape. For the filtered TiO<sub>2</sub> or TiO<sub>2</sub> gel samples with or without adsorbed metal ions, the sample was placed in a sample cell with a rubber spacer and Mylar windows.

**3. Data Analysis.** XAFS data analysis was carried out using standard procedures. Considering only 3% of the TiO<sub>2</sub> is on the surface (see below), TiO<sub>2</sub> nanoparticles with 400 Å diameters were used as a reference for the structure of anatase TiO<sub>2</sub> lattice, where the first-shell Ti–O distance is 1.96 Å with six O atoms, the second-shell Ti–Ti distance is 3.04 Å with four Ti atoms, and the third-shell Ti–O distance is 3.86 Å with 12 O atoms.<sup>16</sup> Five other reference compounds were used to extract structural parameters for the metal complexes. For Cu ions, the structural reference parameters were extracted from the Cu(glycine)<sub>2</sub> complex (Cu–Gly)<sub>2</sub> with a known X-ray structure.<sup>17</sup> Cupric oxide (CuO) was also used as a reference based on its crystal structure.<sup>18</sup> Cu foil was used for characterizing Cu–Cu distances. HgS (black) and HgO were used as references<sup>19,20</sup> for Hg complexes. In most cases, *k*<sup>3</sup> weighting was used, and Fourier transforms were taken between *k* = 3 and 11 Å<sup>–1</sup>.

To demonstrate the effects of the size of the TiO<sub>2</sub> lattice and the locations of absorbing Ti atom on the XAFS spectra, we used the program FEFF6.0 (University of Washington) to simulate the XAFS spectra of TiO<sub>2</sub> anatase lattice. Simulations were carried out with different sizes of the TiO<sub>2</sub> lattice: (1) TiO<sub>6</sub>, (2) Ti<sub>9</sub>O<sub>38</sub>, and (3) Ti<sub>45</sub>O<sub>106</sub> as well as different locations of absorbing Ti atom (on the surface vs in the middle of the lattice). Multiple scatterings were included in the calculations. The maximum scattering path length was set at 9.5, and the maximum number of scattering paths in each route was 8. Because the goal of these simulations is to find the origin of the spectral characteristics of the Ti at different locations in a TiO<sub>2</sub> lattice cluster and the effect of cluster sizes, an ideal anatase lattice structure in the cluster was used, and the Debye–Waller factors were assumed to be zero for simplification.

## III. Results and Discussion

**1. Particle Size Dependence of TiO<sub>2</sub> Nanoparticle Structures.** *Ti Site Structures in TiO<sub>2</sub> Nanoparticles: Surface vs Bulk.* The origin of the unique photocatalytic activities exhibited by nanoparticles of TiO<sub>2</sub> is crucial to understanding the reaction mechanisms, whether it is purely due to the increased surface area or due to distorted sites on the surface or the whole lattice of the particle. Because the XAFS technique detects the local structural details around the X-ray-absorbing atoms, this technique is particularly powerful in determining short-range structures of surface Ti sites in TiO<sub>2</sub> nanoparticles. In studying the surface structure of TiO<sub>2</sub> nanoparticles using XAFS, one faces a challenge of the coexistence of the interior and the surface structures. One way to solve this problem is to systematically measure XAFS spectra of a series of TiO<sub>2</sub> particles with different sizes. As the particle size gets smaller, the fraction of TiO<sub>2</sub> on the surface increases, and the XAFS spectral features that reflect the surface TiO<sub>2</sub> structure become more prominent. In this way, we could distinguish the structural features that arise from the surface layer of TiO<sub>2</sub> from those of the structures associated with bulk TiO<sub>2</sub>.

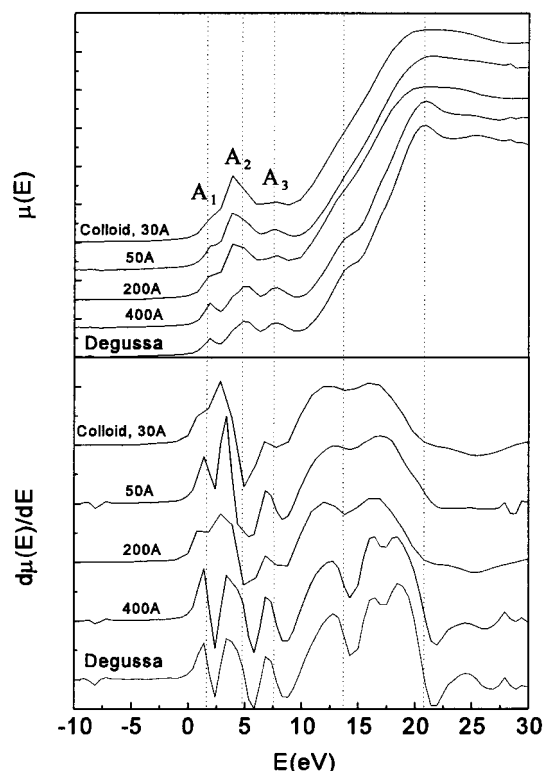


**Figure 1.** Preedge and XANES spectra of  $\text{TiO}_2$  nanoparticles at Ti K-edge ( $E_0 = 4.966$  keV for  $\text{Ti}^0$ ). Top panel: the spectra of  $\text{TiO}_2$  particles with different sizes. Bottom panel: first derivatives of the spectra in the top panel.

**Fractions of Surface  $\text{TiO}_2$  in Nanoparticles.** To analyze the  $\text{TiO}_2$  nanoparticle spectra, we need to estimate the fraction of surface  $\text{TiO}_2$  in a nanoparticle with a specific size. This estimate was made based on the anatase lattice structure,<sup>16</sup> which is the structure determined for  $\text{TiO}_2$  nanoparticles synthesized by controlled hydrolysis of  $\text{TiCl}_4$  at low temperature.<sup>21</sup> The average volume and surface areas of each  $\text{TiO}_2$  were calculated using the dimensions of the anatase unit cell. The approximate average surface area for each  $\text{TiO}_2$  was calculated based on the number density of Ti on different lattice planes and an assumed equal probability of surface exposure for (110), (101), and (011) planes. In other words, the surface area occupied by each  $\text{TiO}_2$  is averaged over these three planes. Based on these parameters, the fraction of the surface  $\text{TiO}_2$  is proportional to  $12.5/d$ , where  $d$  is the diameter of the  $\text{TiO}_2$  nanoparticles in angstroms. Thus, the fraction of exposed  $\text{TiO}_2$  is 3% for 400 Å, 6% for 200 Å, 25% for 50 Å, and 41% for 30 Å diameter particles. However, the surface distortion could be more than one layer deep. Since the 400 Å has only 3% on the surface, we used this as the standard for the bulk anatase.

**Preedge Spectra of Ti K-Edge for  $\text{TiO}_2$  Nanoparticles of Different Diameters.** The preedge structure at the Ti K-edge for  $\text{TiO}_2$  features three peaks:  $A_1$ ,  $A_2$ , and  $A_3$  (see Figure 1). According to previous studies, the origins for  $A_2$  and  $A_3$  are attributed to  $1s \rightarrow 3d$  transitions and designated to  $1s \rightarrow 2t_{2g}$  and  $1s \rightarrow 3e_g$  transitions in an octahedral field, respectively, and the origin for  $A_1$  was assigned to an exciton band<sup>22</sup> or a transition from  $1s \rightarrow 1t_{1g}$  resulting from possible perturbation due to shake-up and shake-off processes.<sup>23</sup> An increase in relative intensity of  $A_2$  has been observed in the  $\text{TiO}_2$  materials with increasing distortion from the octahedral  $\text{TiO}_6$  unit, and an intense single preedge peak has been observed for  $\text{TiO}_2$  with a tetrahedral geometry around Ti.<sup>23–25</sup> Extensive efforts have been made to theoretically calculate the preedge structure of  $\text{TiO}_2$  with a limited number of atoms.<sup>26–28</sup> While the reproduc-

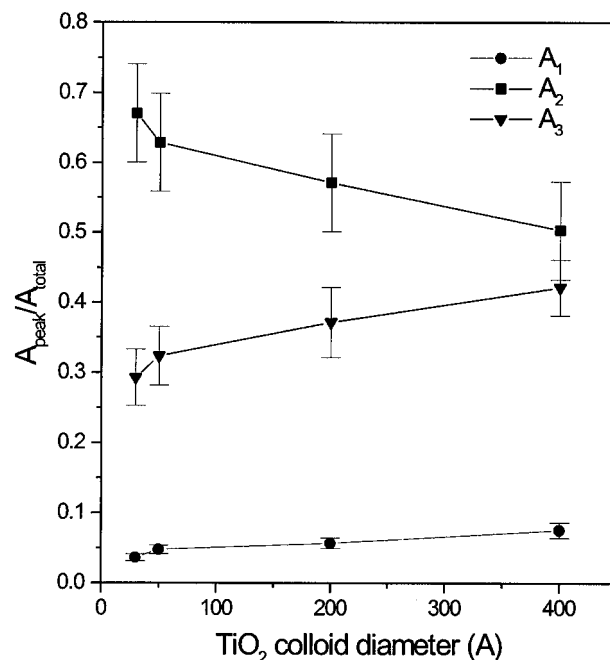


**Figure 2.** Relative intensities of preedge peaks (see text)  $A_1$ ,  $A_2$ , and  $A_3$  as functions of  $\text{TiO}_2$  particle diameters.

tion of the preedge for rutile  $\text{TiO}_2$  is rather successful, that for the anatase  $\text{TiO}_2$  still lacks agreement with the spectral detail.<sup>26</sup> We have observed a systematic increase in the intensity of the  $A_2$  peak with a decrease in particle size (Figure 1), indicating an increasing distortion from the octahedral  $\text{TiO}_6$  unit. As the particle size becomes smaller, more Ti atoms are exposed on the surface of the particle experiencing an anisotropic environment where a Ti atom bonds to inner and outer O atoms simultaneously. This anisotropic environment for the surface Ti atoms may be the cause of the possible distortion around Ti atoms from an octahedral  $\text{TiO}_6$  unit. Meanwhile, the intensity of the  $A_1$  peak decreases as the particle size decreases. However, the fractions of integrated intensities of  $A_1$ ,  $A_2$ , and  $A_3$  as functions of the sizes of the particles seem to correlate with each other (see Figure 2). The most obvious changes occur for particles with diameters less than 50 Å. In other words, the distortion of the lattice consistently increases as the particle size gets smaller. Nevertheless, the preedge of all three transitions is still clearly visible in the spectrum of 30 Å diameter particles even though the  $A_2$  peak dominates. However, this preedge spectrum is significantly different from that for Ti atoms in tetrahedral  $\text{TiO}_4$  sites, where only one sharp peak, about one-half of the white line peak height, was observed.<sup>23</sup> Although the observed  $A_2$  peak enhancement in particles with 30 Å diameter could result from a very small number of tetrahedral sites, the Ti sites in  $\text{TiO}_2$  particles studied here are mostly octahedral. The distortion around Ti is never severe enough that the Ti site becomes tetrahedral as for  $\text{TiO}_2$  in  $\text{SiO}_2$  glass.<sup>23,25</sup>

**XANES of Ti K-Edge for  $\text{TiO}_2$  Nanoparticles of Different Diameters.** Other spectral features in the XANES region (see Figure 1) include a peak around 13.5 eV above the  $A_1$  peak, in the middle of the rising edge. The first derivatives of the XANES spectra for different particle sizes show that the peak diminishes as the particle size is reduced. However, the peak is still visible even for particles with 30 Å diameters. This peak was assigned to the  $1s \rightarrow 4p$  transition.<sup>22</sup> Other peaks in this region, along with those in the XAFS spectra, also significantly broaden as the particle size gets smaller. Two effects could contribute to the observed spectral changes: (1) an increase of the fraction of surface  $\text{TiO}_2$  and (2) the inhomogeneity in the lattice structures in small nanoparticles.

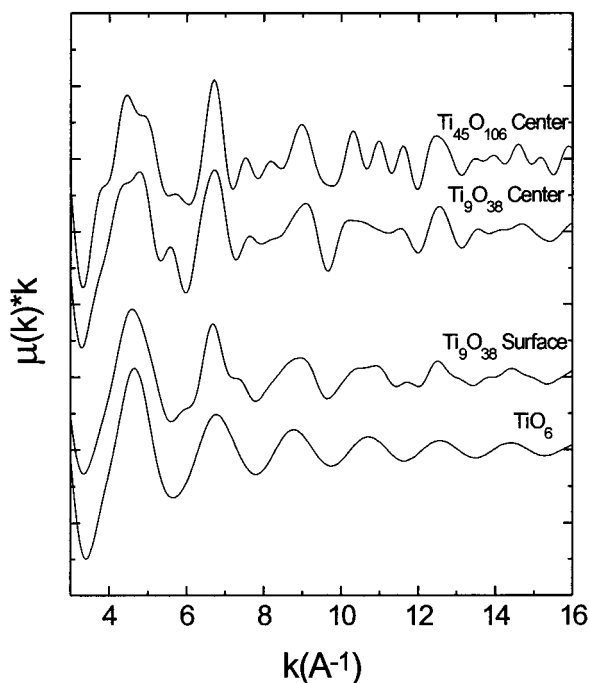


**Figure 3.** Calculated XAFS spectra using FEFF6.0 for TiO<sub>2</sub> lattice with different sizes and different locations of absorbing Ti atom (on the surface or in the center of the cluster).

The first effect above is simulated by calculated XAFS spectra of Ti in TiO<sub>2</sub> anatase clusters of different sizes and at different locations (center or surface) using FEFF 6.0. The results are depicted in Figure 3. When a Ti atom is in an isolated TiO<sub>6</sub> unit surrounded only by a single shell of six O atoms, its XAFS spectrum has a single frequency sinusoidal oscillation without fine features. When an X-ray-absorbing Ti is surrounded by several shells of backscattering atoms, superpositioning of the backscattered photoelectron waves from different shells and the multiscattering produces many fine features in an XAFS spectrum. Therefore, for the Ti atom situated in the center of TiO<sub>6</sub>, Ti<sub>9</sub>O<sub>38</sub>, and Ti<sub>45</sub>O<sub>106</sub>, an increasing complexity in spectral features is observed. When the absorbing Ti atom is moved from the center to the surface in a TiO<sub>2</sub> cluster, part of the multiscattering pathways are truncated, resulting in a spectrum with fewer fine features. Therefore, an increase in the surface fraction of the Ti atom alone could cause the diminishing fine features in XAFS spectra as the TiO<sub>2</sub> particle size decreases. However, the fine spectral features for the Ti atom could also be compromised by heterogeneous broadening when there is an inhomogeneity in the local structure around Ti atoms. The static disorder in the Ti-to-other atom distances and the bond angles will cause the heterogeneous broadening of the spectra. Because the XAFS effect is due to short-range structure around the X-ray-absorbing atoms, the broadening itself suggests inhomogeneity of the local structure, rather than loss of the coherence due to a size effect observed in X-ray diffraction.

XAFS results alone are not sufficient to distinguish between the two possible causes of the broadening of spectral features, but the analysis of XAFS spectra presented in the following section could provide the structural information that is uniquely present in TiO<sub>2</sub> nanoparticles.

**XAFS Spectra of TiO<sub>2</sub> Colloidal Particles with Different Diameters.** The XAFS spectra for TiO<sub>2</sub> colloid particles of different diameters are shown in Figure 4. As a general trend, the oscillation amplitude in the spectra reduces as the particle size decreases. Meanwhile, the oscillations also broaden, and fine structure is lacking in the smaller particles, similar to the results in the XANES region. The fine structure observed in

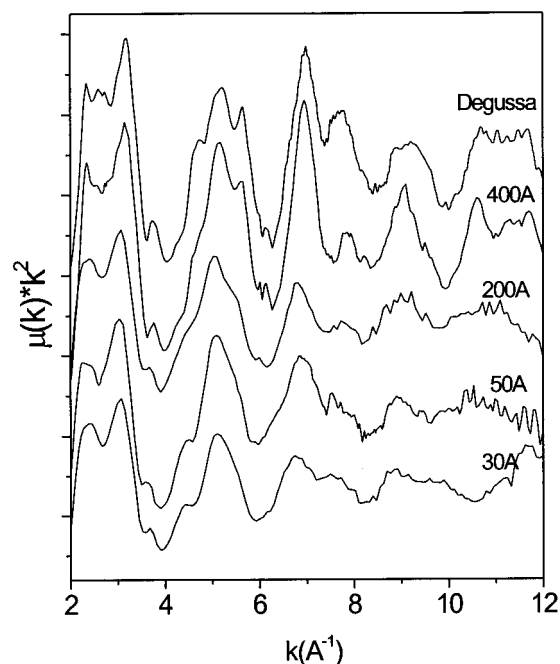


**Figure 4.** XAFS spectra of TiO<sub>2</sub> nanoparticles with different diameters.

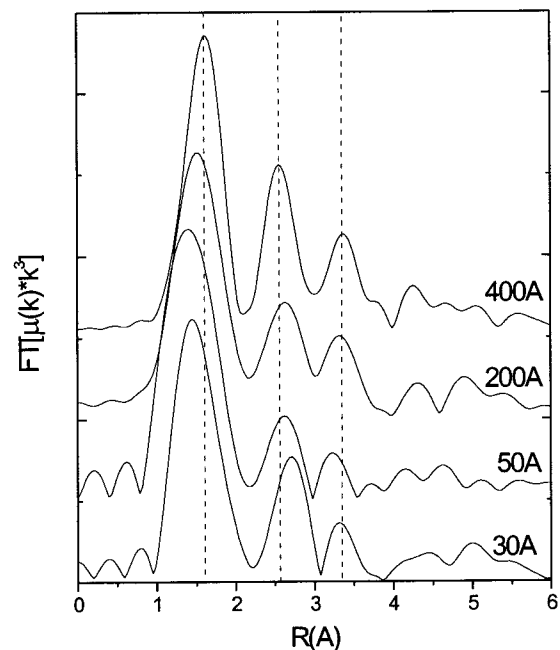


**Figure 5.** FT-XAFS spectra of TiO<sub>2</sub> nanoparticles with different diameters.

400 Å diameter particles is significantly broadened in 200 Å diameter particles, although the fraction of surface TiO<sub>2</sub> changes from 3% to 6%. This observation indicates that the observed spectral changes are not entirely due to the increase of the surface TiO<sub>2</sub>, and a global disorder throughout the entire particle may also occur when the particle size reaches a certain limit. In addition to the damping of the oscillation amplitudes, the oscillation patterns of the spectra in the high- $k$  region also show substantial differences as a function of particle size. This implies that there are structural differences other than the differences in the Debye–Waller factor alone between the particles with different sizes. This can be seen more clearly in the FT-XAFS spectra in Figure 5. The bond distance of Ti to the first-shell O atom varies with the size of the particles. The FT window is taken from  $k = 3$ –11 for all the spectra. The first-shell fit for TiO<sub>2</sub> particles with 200, 50, and 30 Å diameters

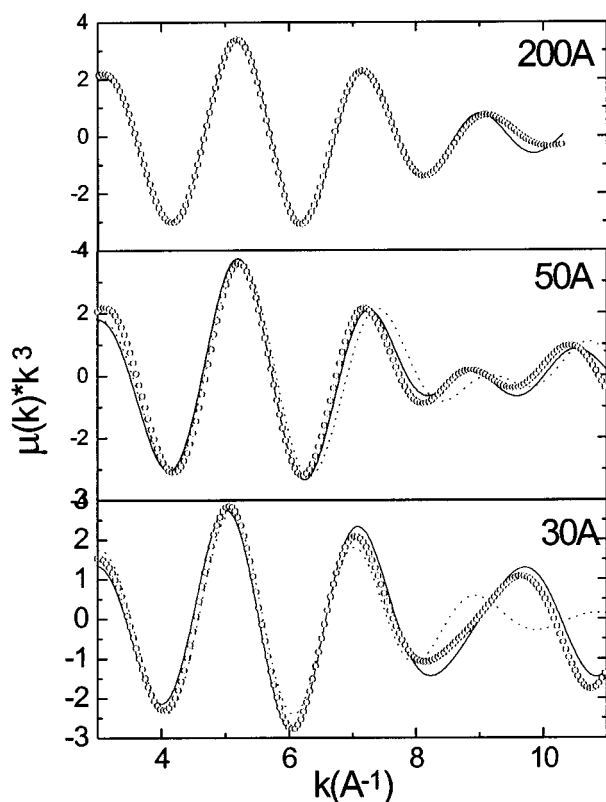


**Figure 6.** First-shell Ti–O distance fitting for  $\text{TiO}_2$  particles with different sizes. One shell model fits well for 200 Å particles (solid line in top panel), but not for 50 and 30 Å particles (middle and bottom panels, dotted lines, respectively). However, two-shell model fits improved significantly the fits (solid lines).

is presented in Figure 6. Even for 200 Å  $\text{TiO}_2$  colloid particles, the width of the first peak is broader than that of 400 Å particles, and the average distance of the first-shell Ti–O bonds is  $1.92 \pm 0.02$  Å with a relatively large  $\sigma$ , instead of  $1.95 \pm 0.02$  Å as in the 400 Å particles. A single-shell model is not adequate to fit the first-shell Ti–O distance in 50 Å particles. However, a two-shell model with 17% of the first-shell Ti–O distance of  $1.77 \pm 0.04$  Å and a longer Ti–O distance of  $1.94 \pm 0.02$  Å for the remaining 83% provides a reasonable fit. The first shell of  $\text{TiO}_2$  particles with 30 Å diameters has a slightly higher fraction (20%) of Ti–O with a distance of  $1.84 \pm 0.04$  Å, and the remaining Ti–O has a distance of  $1.99 \pm 0.02$  Å. The fits for the second-shell Ti–Ti distances and the third-shell Ti–O distances are shown in Table 1. The coordination numbers are still within the experimental error for the 200 Å particles, but the second- and third-shell coordination numbers are reduced for 30 and 50 Å diameter particles. Simultaneous reduction of the second-shell coordination number and the size of the particles suggests a correlation between the two trends. If the coordination number reduction in small nanoparticles is due to the surface  $\text{TiO}_2$  alone, the reduced fractions for the second and third shells should be the same, because the surface Ti loses the two shells simultaneously. However, disorder in the lattice in small particles would cause only the reduction in the third and higher shells because of the heterogeneous broadening. Our results show that the lost fraction of the third shell is 58% and 67%, whereas that for the second shell is 20% and 38% for the particles with 30 and 50 Å diameters, respectively. This extra 30–40% loss of the third-shell coordination numbers compared to those of the second shell could be from the disorder of the lattice structures, such as the “corner effect” where the distortion is due to the large curvature of the particle surface.

**TABLE 1: XAFS Fitting Results for  $\text{TiO}_2$  Colloids Particles<sup>a</sup>**

diameter (Å)	shell	<i>N</i>	<i>R</i> (Å)	$\sigma^2$ (Å <sup>2</sup> ) <sup>b</sup>
400 (ref)	1	6.0	1.96	
	2	4.0	3.04	
	3	12.0	3.86	
200	1	$6.4 \pm 0.5$	$1.92 \pm 0.02$	0.010
	2	$4.6 \pm 0.5$	$3.09 \pm 0.04$	0.006
	3	$12 \pm 2$	$3.87 \pm 0.04$	0.010
50	1	$5.0 \pm 0.5$	$1.94 \pm 0.02$	0.003
	1	$1.0 \pm 0.2$	$1.77 \pm 0.02$	–0.006
	2	$2.5 \pm 0.5$	$3.09 \pm 0.04$	0.005
30	3	$4 \pm 1$	$3.77 \pm 0.04$	0.006
	1	$4.0 \pm 0.5$	$1.99 \pm 0.02$	0.003
	1	$0.8 \pm 0.2$	$1.84 \pm 0.02$	–0.006
	2	$3.2 \pm 0.5$	$3.13 \pm 0.04$	0.008
	3	$5 \pm 1$	$3.83 \pm 0.04$	0.007

<sup>a</sup>  $\text{TiO}_2$  particles of 400 Å diameters were used as the reference compound, with the assumption that they have the same lattice structure as anatase. The first shell has Ti–O distance with  $N = 6$ ,  $R = 1.95$  Å, the second shell has Ti–Ti distance with  $N = 4$ ,  $R = 3.04$  Å, and the third shell has Ti–O distance with  $N = 12$ ,  $R = 3.86$  Å. <sup>b</sup> Relative to 400 Å diameter  $\text{TiO}_2$ .

The first-shell Ti–O peak in the FT-XAFS spectra for 30 and 50 Å diameter particles fits a two-shell model, where one Ti–O distance is close to 1.95 Å and the other 0.1–0.2 Å shorter (see Table 1). The necessity of introducing the second Ti–O distance in the smaller particles suggests that the shorter Ti–O distance is from the exposed Ti–O. The fact that the second-shell Ti–Ti peak and the third-shell Ti–O peak do not need the second distance in the fitting supports the idea that the shorter first Ti–O distance is from the surface Ti–OH, rather than from the disorder of the lattice.

In summary of this section, our XAFS measurements at the Ti K-edge show shorter Ti–O distances for surface  $\text{TiO}_2$ , resulting from Ti–OH bonding. Minor disorder of the lattice in smaller nanoparticles was observed based on the additional loss of the third-shell O atom and the relative intensity changes as a function of particle size for the  $A_1$ ,  $A_2$ , and  $A_3$  peaks. However, the Ti sites largely remain octahedral even in the 30 Å diameter particles. Because the interfacial electron/hole transfer occurs via surface Ti or O atoms, the observed structural changes around the surface Ti atoms in small  $\text{TiO}_2$  particles could be responsible for the unique photochemistry displayed in nanoparticle-assisted reactions.

**2. Photoreduction of Metal Ions on Modified  $\text{TiO}_2$  Surfaces.** There have been a number of studies of photoreduction of metal ions on  $\text{TiO}_2$  surfaces.<sup>7–11</sup> The modification of the  $\text{TiO}_2$  nanoparticle surfaces with adsorbents has made some photoreductions of metal ions feasible or improved the efficiency of the reduction.<sup>13</sup> However, several questions arise regarding these photoreactions: (1) are metal ions reduced to the metal on the  $\text{TiO}_2$  surface, (2) does the surface adsorbent affect the efficiency of the putative photoreduction, (3) what are the structures of the metal complexes involved in the reaction, and (4) what roles do the metal complexes play in the putative photoreduction? The surface modifiers were chosen based on their capability of binding both metal ions and the  $\text{TiO}_2$  surface, acting only as a bridging agent. We present XAFS results for photoreactions of  $\text{Cu}^{2+}$  and  $\text{Hg}^{2+}$  ions in  $\text{TiO}_2$  surfaces with and without modification. The results provide information on the metal oxidation states and geometry of the metal complexes.

**Photoreduction of  $\text{Cu}^{2+}$  on  $\text{TiO}_2$  Surface.** A series of XAFS spectra were taken at the Cu K-edge for a mixture of 0.01 M  $\text{Cu}^{2+}$  ions (from copper acetate) and  $\text{TiO}_2$  nanoparticles (50 Å diameters) with and without the surface modifier Ala after different lengths of time of xenon lamp illumination. Since the

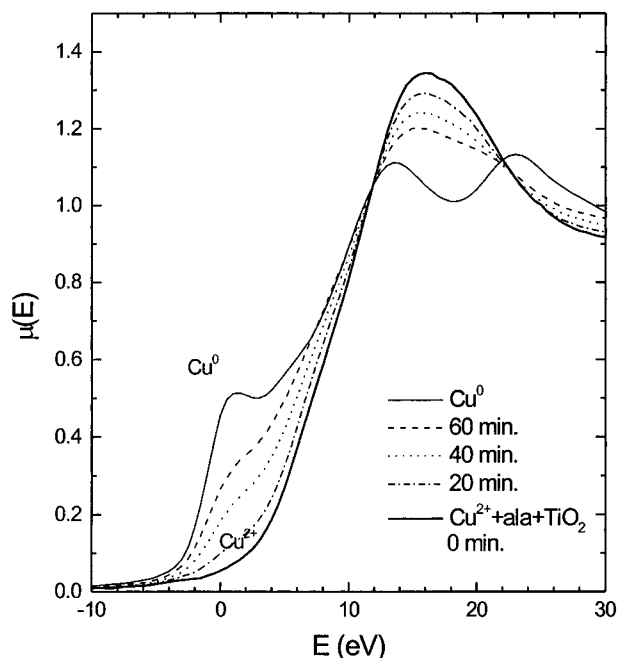


**Figure 7.** Cu K-edge (8.979 keV) XANES spectra for copper metal and Cu<sup>2+</sup>/Ala/TiO<sub>2</sub> at different illumination times.

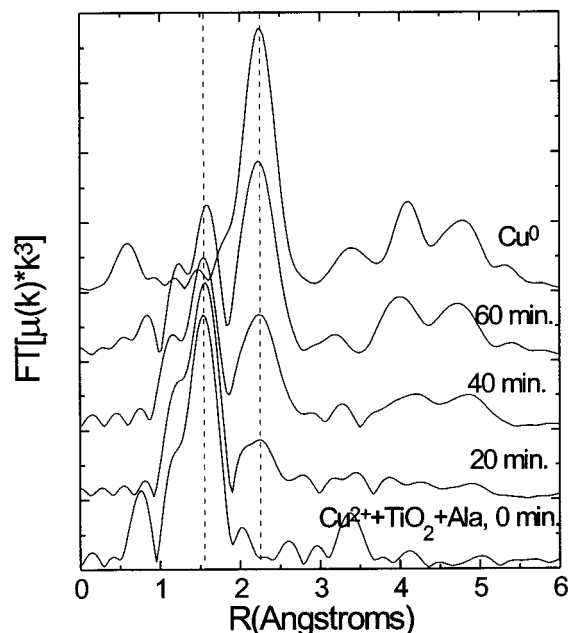


**Figure 8.** FT-XAFS spectra for copper metal and Cu<sup>2+</sup>/Ala/TiO<sub>2</sub> at different illumination times.

lifetimes of photogenerated charge carriers are very short due to rapid recombination, only reactions with adsorbed species lead to an efficient charge separation. We have found that with the presence of Ala a significant amount of adsorbed Cu<sup>2+</sup> was reduced and the amount of Cu<sup>0</sup> increased with the time of illumination, whereas little photoreduction was observed for the same sample without Ala. These results are shown in both XANES (Figure 7) and FT-XAFS (Figure 8) spectra. Before illumination, the FT-XAFS spectrum (not corrected for phases) for the Cu<sup>2+</sup>/TiO<sub>2</sub>/Ala mixture has a dominant peak between  $R = 1$  and  $2$  Å and a minor peak at  $3.3$  Å. These peaks are assigned to backscattering from O or N atoms from H<sub>2</sub>O or Ala molecules directly chelated with Cu atoms and to the O atoms of the second layer of solvated H<sub>2</sub>O, respectively.<sup>17</sup> After illuminating for 20 min, a new peak appeared between  $R = 2.0$  and  $2.5$  Å at the same position as the first shell in a copper foil

**TABLE 2: XAFS Fitting Results for Cu–Alanine Complexes during Photoreduction on TiO<sub>2</sub> Colloid Surfaces<sup>a</sup>**

illumination time (min)	shell <sup>b</sup>	$N$	$R$ (Å)	rel $\sigma^2$ (Å)
0	Cu <sup>2+</sup>	$4.2 \pm 0.5$	$1.96 \pm 0.02$	0.001
20	Cu <sup>2+</sup>	$3.8 \pm 0.5$	$1.96 \pm 0.02$	0.002
20	Cu <sup>0</sup>	$0.8 \pm 0.2$	$2.58 \pm 0.02$	−0.002
40	Cu <sup>2+</sup>	$3.3 \pm 0.5$	$1.96 \pm 0.02$	0.003
40	Cu <sup>0</sup>	$1.7 \pm 0.5$	$2.57 \pm 0.02$	−0.001
60	Cu <sup>2+</sup>	$2.9 \pm 0.5$	$1.97 \pm 0.02$	0.004
60	Cu <sup>0</sup>	$2.6 \pm 0.5$	$2.56 \pm 0.02$	−0.001

<sup>a</sup> Reference compounds, Cu–(Gly)<sub>2</sub>, Cu–O(N) distance  $1.96$  Å,  $N = 4$ , and Cu foil, Cu–Cu distance  $2.56$  Å,  $N = 12$ . <sup>b</sup> The shells here are defined based on Figure 8, where the first major peak is from Cu<sup>2+</sup> and the second peak is from Cu<sup>0</sup>.

spectrum (top trace, Figure 8). As the illumination proceeded, this newly appearing peak grew at the expense of the first Cu<sup>2+</sup>–O (or Cu<sup>2+</sup>–N) peak, and three other peaks appeared between  $R = 3$  and  $5$  Å, also at the same position as those observed in the copper foil spectrum (top trace, Figure 8). Appearance of these four peaks during the illumination period clearly confirmed the photoreduction of Cu<sup>2+</sup> as well as the formation of Cu<sup>0</sup> clusters. After illuminating for 60 min, ~50% of Cu<sup>2+</sup> adsorbed on the TiO<sub>2</sub> nanoparticle surfaces was photoreduced. Small metal copper particles became visible at that time. The XAFS data analyses for the first peak (Cu<sup>2+</sup>) and the second peak (Cu<sup>0</sup>) are listed in Table 2. A Cu–glycine (Cu–Gly)<sub>2</sub> complex<sup>17</sup> with an average Cu–O and Cu–N distance of  $1.96 \pm 0.02$  Å, and a copper foil with a nearest Cu–Cu distance of  $2.56 \pm 0.02$  Å,<sup>29</sup> were used as reference structures. Although the Cu–Cu distances beyond the first shell are clearly shown through the cluster of the peaks between  $R = 3$  and  $5$  Å in the spectra after 40 min illumination, they could appear after shorter illumination periods at a concentration that is too low to detect. The growth of the Cu<sup>0</sup> with illumination time can also be monitored by XANES and XAFS spectra in Figures 7 and 8. Photoreduction efficiency of Cu<sup>2+</sup> on TiO<sub>2</sub> colloid surfaces in the presence of copper acetate only was very low, and little convincing evidence of Cu<sup>0</sup> from XAFS spectra could be observed after prolonged illumination (see the second spectrum from the top in Figure 9).

The reoxidation of Cu<sup>0</sup> in the mixture with TiO<sub>2</sub>/Ala was observed after the photoreduced sample was exposed to air and was recorded by XAFS (not shown) in a similar fashion as the photoreduction. As the photoreduced sample was exposed to air, the Cu<sup>0</sup> peaks in FT-XAFS spectra gradually diminished while the Cu<sup>2+</sup> peaks appeared, a reverse process of the photoreduction observed earlier.

To know why the formation of the Cu–adsorber complex affects the photoreduction efficiency and how the structures surrounding Cu in the cases with and without Ala differ, FT-XAFS spectra for various Cu<sup>2+</sup> complexes (Figure 9) were analyzed. The spectrum for the Cu–Ala complex (Cu–[NHCHCH<sub>3</sub>COO])<sub>2</sub>, Cu–Ala<sub>2</sub>, second from the bottom) shows not only the first shell but also two other shells at  $R \sim 2.4$  and  $3.5$  Å. This spectrum is virtually identical with that previously observed for the Cu–Gly<sub>2</sub> complex (Lytle, private communication). Thus, the Cu–Gly<sub>2</sub> complex was used as the reference compound for Cu–Ala<sub>2</sub> structural determination. The X-ray structure of the Cu–Gly<sub>2</sub> complex shows that the Cu<sup>2+</sup> atom chelated directly with one of the O atoms of the carboxyl group and the N atom of the amino group from each of the two Gly molecules, forming square-planar, two five-membered rings.<sup>17</sup> The mean Cu–O distance is  $1.97 \pm 0.02$  Å, and the mean Cu–N distance is  $1.96 \pm 0.02$  Å. According to the X-ray structure, the second shell in the spectrum of the Cu<sup>2+</sup>–Ala

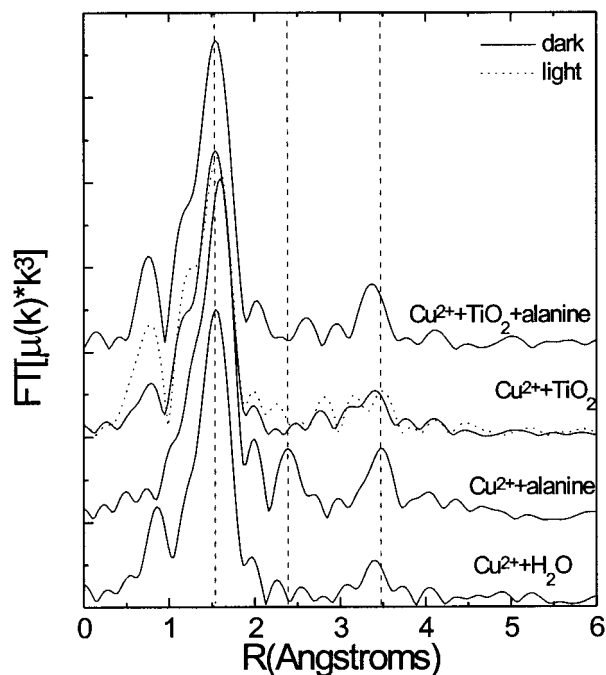


**Figure 9.** FT-XAFS spectra for different  $\text{Cu}^{2+}$  complexes.

complex in Figure 9 is from the  $\alpha$ -carbon and carboxyl carbon atoms. The third shell in the spectrum is from a combination of the methyl carbon and oxygen (not chelated to the Cu atom) as well as the second layer of solvated  $\text{H}_2\text{O}$ .<sup>17</sup> The third-shell peak in the vicinity of  $R = 3.5$  Å appears in other spectra in Figure 9 as well. In most of the hydrated transition-metal ions, this peak is due to backscattering from the second O atom in a configuration of metal–O–H...O–H, indicating the solvated  $\text{H}_2\text{O}$  layer around  $\text{Cu}^{2+}$ .<sup>30</sup>

The second-shell peak (at  $R \sim 2.4$  Å without phase correction in Figure 9) is only present in the Cu–Ala<sub>2</sub> complex, which indicates that the structure of the complex is well-defined by the chelation with two five-membered rings. When  $\text{TiO}_2$  was added, this second-shell peak disappeared, suggesting that the original five-membered ring structure in the  $\text{Cu}^{2+}$ –Ala<sub>2</sub> complex has been destroyed. If one of the two five-membered rings survives, the second shell should still be present. Two possible structures of the Cu surroundings in the  $\text{Cu}^{2+}/\text{TiO}_2/\text{Ala}$  mixture are suggested based on the experimental observation of the similarity between the FT-XAFS spectra of  $\text{Cu}^{2+}/\text{H}_2\text{O}$  and  $\text{Cu}^{2+}/\text{TiO}_2/\text{Ala}$ : (1)  $\text{Cu}^{2+}$  binds to only one end of each Ala and to O atoms of surface Ti; (2)  $\text{Cu}^{2+}$  binds only on  $\text{TiO}_2$  surfaces via dynamic electrostatic interactions. Both ways of binding will cause disappearance of the second-shell structure in the FT-XAFS spectrum. However, the former is considered more plausible because only when  $\text{Cu}^{2+}$  binds to Ala can the photoelectron that is transported away from the  $\text{TiO}_2$  surface be effectively transferred to  $\text{Cu}^{2+}$ . Alanine has the same electrochemical properties as the acetate used in both solutions ( $E^\circ(\text{Ala}/\text{Ala}^+) = E^\circ(\text{CH}_3\text{COO}^-/\text{CH}_2\text{CO}) = 2.2$  V vs NHE).<sup>31</sup> Therefore, only the difference in binding between  $\text{Cu}^{2+}$  and the  $\text{TiO}_2$  nanoparticle surface leads to the observed difference in photoreduction efficiency when  $\text{TiO}_2$  is present.

The other important question is whether  $\text{Cu}^+$  is present during the photoreduction. It has been reported that photoreduction of  $\text{Cu}^{2+}$  at the  $\text{TiO}_2$  surface produces a mixture of  $\text{Cu}_2\text{O}$  and  $\text{Cu}^0$ .<sup>8</sup> The copper K-edge is sensitive to the oxidation states of the metal ions, and  $\text{Cu}^+$  has a preedge structure distinct from that of  $\text{Cu}^{2+}$ . The  $\text{Cu}^+$  K-edge is between that for  $\text{Cu}^0$  and  $\text{Cu}^{2+}$  at about 5 eV above the  $\text{Cu}^0$  K-edge.<sup>32</sup> Therefore, we expect that an edge structure would show up at this energy

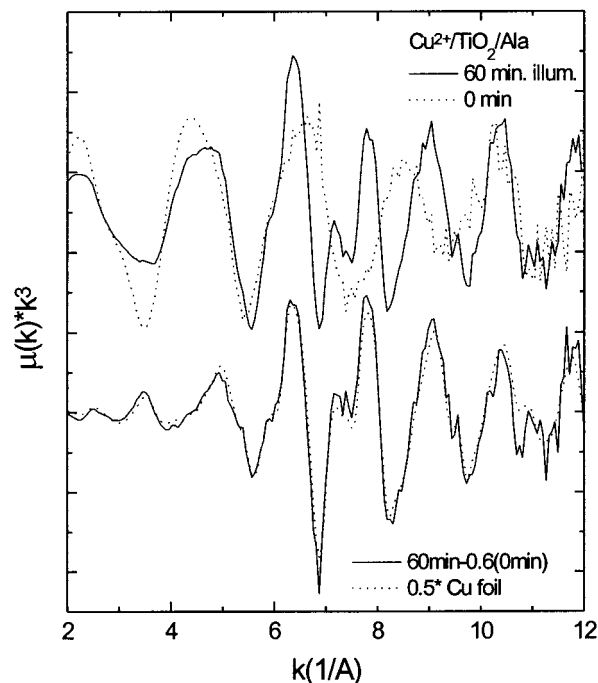


**Figure 10.** Top: XAFS spectra of  $\text{Cu}^{2+}/\text{Ala}/\text{TiO}_2$  before and after 60 min illumination. Bottom: XAFS spectrum of copper foil (dotted) and a difference spectrum from subtracting 60%  $\text{Cu}^{2+}/\text{Ala}/\text{TiO}_2$  spectrum without illumination from that of a mixture after 60 min illumination. The bottom two spectra overlap well, indicating the remaining spectrum is from the  $\text{Cu}^0$  photoreduced from initial  $\text{Cu}^{2+}$ .

region if  $\text{Cu}^+$  is present. No extra peak was observed in addition to the peaks for  $\text{Cu}^0$  and  $\text{Cu}^{2+}$ . To see whether  $\text{Cu}^+$  is present, we examined spectra from the following: (1) Cu foil, (2)  $\text{Cu}^{2+}/\text{TiO}_2/\text{Ala}$  with no illumination, and (3)  $\text{Cu}^{2+}/\text{TiO}_2/\text{Ala}$  with 60 min illumination. If there is no  $\text{Cu}^+$  species present, the spectrum from (3) should be a mixture of the spectra from (1) and (2). Otherwise, there could be extra spectral features representing the third Cu species. Within the error of the XAFS, we did not find the third species. The remaining spectrum after we subtracted 60% of  $\text{Cu}^{2+} + \text{TiO}_2 + \text{Ala}$  without light from the spectrum of  $\text{Cu}^{2+}/\text{TiO}_2/\text{Ala}$  with 60 min illumination resembles the Cu foil spectrum well (see Figure 10). Our results show that 40–50%  $\text{Cu}^{2+}$  adsorbed has been reduced after 1 h illumination. Although a small amount of  $\text{Cu}^+$  could be present in the mixture, this amount is beyond our detection limit. Therefore, we can conclude that no observable amount of  $\text{Cu}^+$  is present in the system during the light-induced reduction on  $\text{TiO}_2$  colloid surfaces.

**Photoreduction of  $\text{Hg}^{2+}$  on  $\text{TiO}_2$  Surface with and without Thiolactic Acid.** Photoreduction of  $\text{Hg}^{2+}$  on  $\text{TiO}_2$  surfaces was examined by XAFS in a similar fashion as for  $\text{Cu}^{2+}$  photoreduction. The formation of  $\text{Hg}^0$  on  $\text{TiO}_2$  colloid surfaces was monitored at the Hg L<sub>III</sub>-edge. Mixtures of 0.01 M  $\text{Hg}^{2+}/\text{TiO}_2$  with and without 0.02 M thiolactic acid (TLA,  $\text{CH}_3\text{CHSHCOOH}$ ) were illuminated for 1 h. We added 0.1 M methanol as a hole scavenger to the sample without TLA, because its oxidation potential is the same as that of TLA ( $E^\circ(\text{TLA}/\text{TLA}^+) = E^\circ(\text{CH}_3\text{OH}/\text{CH}_2\text{O}) \approx 1.2$  V vs NHE) and it does not chelate with  $\text{Hg}^{2+}$  ions. Figure 11 shows XANES spectra of the filtered mixture before and after illumination, along with the spectra of other relevant Hg complexes. The XANES spectra of  $\text{Hg}^{2+}/\text{TLA}$  with and without  $\text{TiO}_2$  before the illumination are very similar and distinctively different from that of  $\text{Hg}^{2+}/\text{TiO}_2$ , indicating direct chelation of TLA with  $\text{Hg}^{2+}$ . The presence of  $\text{Hg}^{2+}$  in aqueous solution is characterized by a peak in the middle of the rising edge at 4.2 eV, and that peak is absent in the  $\text{Hg}^0$  spectrum.

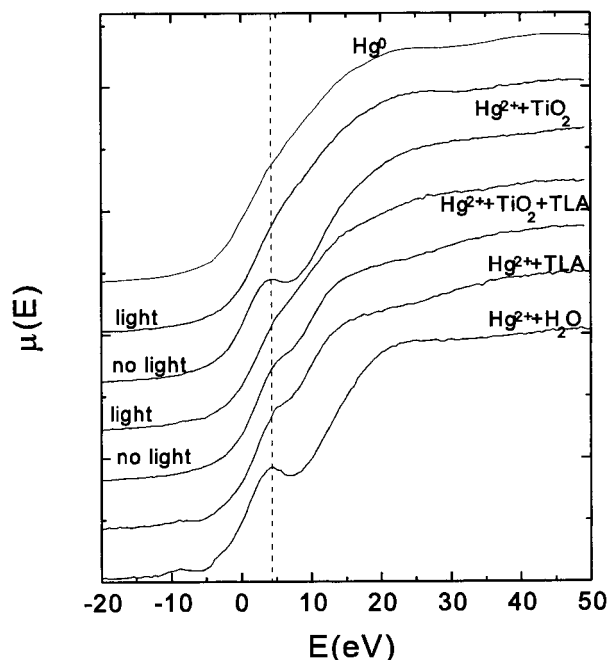


**Figure 11.** Hg L<sub>III</sub>-edge (12.284 keV) XANES spectra of different Hg-containing samples (indicated when photoillumination is applied).

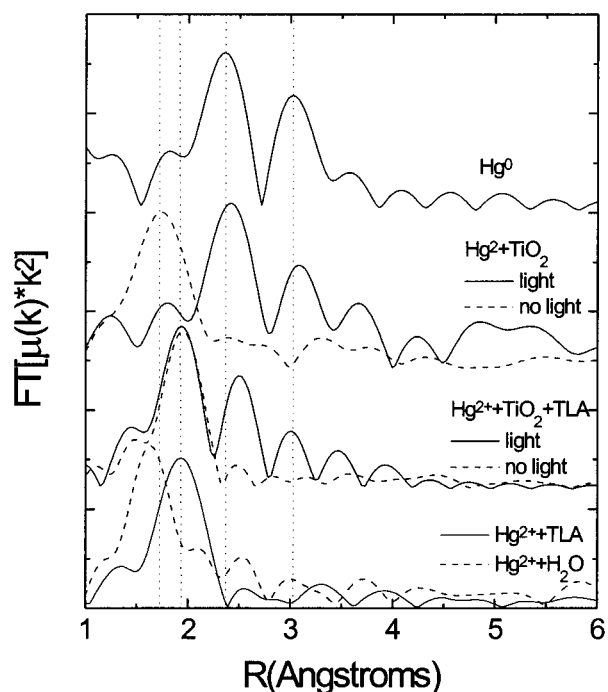


**Figure 12.** FT-XAFS spectra of XANES spectra of different Hg-containing samples (indicated when photoillumination is applied). The spectra were rescaled to align them at the most intense peak of each spectrum.

On the basis of this observation, we found that the XANES spectrum of adsorbed Hg<sup>2+</sup> on TiO<sub>2</sub> (methanol was added) after 1 h illumination had essentially the same spectral features as Hg<sup>0</sup>. Thus, almost all the Hg<sup>2+</sup> adsorbed was reduced. However, the photoreduction of the adsorbed Hg<sup>2+</sup> is incomplete when TLA is present (without methanol) under similar experimental conditions, because the peak at ~4.2 eV is still visible.

This difference in reaction efficiencies for the two systems can also be demonstrated by FT-XAFS spectra in Figure 12. Before the 1 h photoillumination in Hg<sup>2+</sup>/TiO<sub>2</sub> with methanol, the first-shell peak was at  $R = 1.72$  Å (no phase correction), which is characteristic of Hg<sup>2+</sup> surrounded by O atoms in

**TABLE 3: Structural Parameters of Hg Complexes<sup>a</sup>**

complex	shell (atom)	<i>N</i>	<i>R</i> (Å)	rel <i>σ</i> <sup>2</sup> (Å <sup>2</sup> )
Hg <sup>2+</sup> /H <sub>2</sub> O	1 (O)	2.9 ± 0.5	2.02 ± 0.02	0.004
Hg <sup>2+</sup> /TLA	1 (S)	3.8 ± 0.5	2.35 ± 0.02	-0.004
Hg <sup>2+</sup> /TiO <sub>2</sub> (light)				
Hg <sup>2+</sup> /TiO <sub>2</sub> (dark)	1 (O)	2.9 ± 0.5	2.05 ± 0.02	0.004
Hg <sup>2+</sup> /TiO <sub>2</sub> /TLA (light)	1 (S)	1.2 ± 0.4	2.39 ± 0.03	-0.005
Hg <sup>2+</sup> /TiO <sub>2</sub> /TLA (light)	2 (S)	0.4 ± 0.2	2.60 ± 0.03	-0.008
Hg <sup>2+</sup> /TiO <sub>2</sub> /TLA (dark)	1 (S)	2.1 ± 0.5	2.39 ± 0.02	-0.009
Hg <sup>2+</sup> /TiO <sub>2</sub> /TLA (dark)	2 (O)	0.7 ± 0.3	2.04 ± 0.04	0.005

<sup>a</sup> The reference compounds used here are HgO for Hg–O shell and HgS(black) for Hg–S shell. Hg–O distance in HgO is 2.03 Å with a coordination number of 2, and Hg–S distance in HgS(black) is 2.53 Å with a coordination number of 4.

solvated H<sub>2</sub>O or surface O atoms in TiO<sub>2</sub> nanoparticles. After 1 h photoillumination, this peak almost completely disappeared, while a group of peaks that resemble those in Hg<sup>0</sup> appeared, indicating an almost 100% conversion from Hg<sup>2+</sup> to Hg<sup>0</sup>. In the Hg<sup>2+</sup>/TiO<sub>2</sub>/TLA system without methanol, the first-shell peak representing Hg<sup>2+</sup> is shifted to 1.93 Å (no phase correction), indicating a different ligation structure of Hg<sup>2+</sup>. Over 50% of this peak remained after 1 h photoillumination, while the Hg<sup>0</sup> peaks grew. The FT-XAFS spectra for the Hg<sup>2+</sup>/TiO<sub>2</sub>/TLA system after illumination indicated that less than 50% Hg<sup>2+</sup> was converted to Hg<sup>0</sup>. This is consistent with current doubling mechanisms in the presence of methanol, previously described in the literature.<sup>32,33</sup> As a current-doubling reagent, methanol is expected to double the efficiency of photoreduction compared to other reagents with similar redox potentials. However, less than 50% Hg<sup>2+</sup> photoreduction with TLA suggests that TLA does not enhance the reaction efficiency as Ala in the Cu<sup>2+</sup> photoreduction case.

Figure 12 also shows the FT-XAFS spectra (without phase correction) of various Hg complexes along with the Hg<sup>0</sup> spectrum. The positions of the first-shell atoms for Hg<sup>2+</sup>/TLA and Hg<sup>2+</sup>/H<sub>2</sub>O are drastically different. The shorter first-shell distance in the Hg<sup>2+</sup>/H<sub>2</sub>O spectrum is from solvation of Hg<sup>2+</sup> in water and chelation with O atoms, whereas the longer first shell in the Hg<sup>2+</sup>/TLA spectrum is an indication of the Hg–S bond in this complex. When TiO<sub>2</sub> was added, the spectrum of the Hg<sup>2+</sup>/TLA complex was largely retained. This situation differs from that in the Cu<sup>2+</sup>–Ala complex where the structure of the complex is significantly altered when TiO<sub>2</sub> is added.

To find out how TLA affects the photoreduction efficiency, we need to examine various structures of Hg complexes. We used HgO and HgS (black) as the reference compounds. The former has a zigzag chain structure, where Hg and O alternate.<sup>20</sup> Each Hg has two O atoms as the nearest neighbors, and the Hg–O distance is 2.03 Å. Each Hg in black HgS has four tetrahedral neighboring S atoms, and the Hg–S distance is 2.53 Å.<sup>19</sup>

Using these reference compounds, Table 3 lists the structural parameters for several Hg complexes. Since the Hg–O distance is ~2.0 Å and the Hg–S distance varies from 2.3 to 2.5 Å, and the phases of O and S backscattering differ significantly, the atomic species chelated to Hg can be distinguished. Hg<sup>2+</sup> in H<sub>2</sub>O has an average first-shell Hg–O distance of 2.02 Å. In the presence of TiO<sub>2</sub>, this Hg–O distance became slightly longer, 2.05 Å. This result suggests a direct binding of Hg on TiO<sub>2</sub> surfaces. Hg<sup>2+</sup> in Hg<sup>2+</sup>/TLA has a coordination number of 3–4 and a Hg–S distance of 2.35 Å, shorter than the Hg–S distance in HgS. The data cannot be fit using the Hg–O



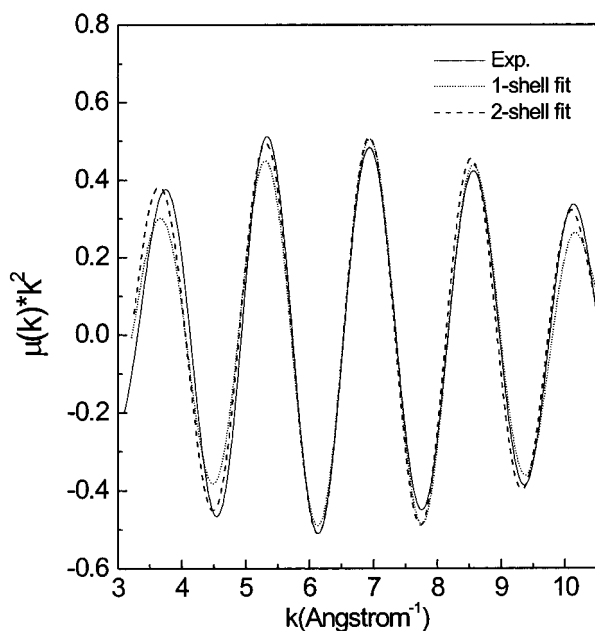


Figure 13. Fits for the first shell in  $\text{Hg}^{2+}/\text{TiO}_2/\text{TLA}$  complex.

distance and the O backscattering phase from HgO as reference parameters. Thus, the chelated atoms in the Hg–TLA complex are most likely S atoms from TLA molecules, and only the S end of TLA binds to Hg, unlike the Cu–Ala complex where both functional groups from each alanine participate in the chelation.<sup>17</sup> This agrees with Hg–S distances observed in other Hg complexes with small organic molecules.<sup>34,35</sup>

The first peak in the FT-XAFS spectrum of the  $\text{Hg}^{2+}/\text{TiO}_2/\text{TLA}$  complex fits much better with a two-shell model, Hg–S at 2.39 Å and Hg–O at 2.04 Å (see Figure 13). The coordination number ratio of Hg–S and Hg–O is 2.1/0.7, approximately 3:1, indicating that one of the TLAs may be replaced by a surface O atom from  $\text{TiO}_2$ . After 1 h illumination, the Hg nearest neighbors in  $\text{Hg}^{2+}/\text{TiO}_2/\text{TLA}$  can be fit to two S shells with a relative ratio of 3:1 and Hg–S distances of 2.39 and 2.60 Å, respectively. Thus, these two distances may be from Hg–S that bonds to TLA and possible formation of HgS, where Hg–S is 2.54 Å. The next-nearest neighbor of Hg in  $\text{Hg}^{2+}/\text{TiO}_2/\text{TLA}$  after photoillumination is Hg having an Hg–Hg distance as in  $\text{Hg}^0$  (see Figure 12).

In summary of this section, the products of the photoillumination of  $\text{Cu}^{2+}$  or  $\text{Hg}^{2+}$  on  $\text{TiO}_2$  nanoparticle surfaces with and without surface adsorbers were analyzed with XAFS. Alanine dramatically enhanced photoreduction of Cu on  $\text{TiO}_2$  nanoparticle surfaces, whereas thiolactic acid did not enhance or even hindered Hg photoreduction. Although both surface adsorbers chelate with the metal ions in the absence of  $\text{TiO}_2$  nanoparticles, this chelation is drastically changed in the Cu–Ala complex but is largely retained in the Hg–TLA complex when  $\text{TiO}_2$  is present. This difference could be explained as follows. First, in the CuAla<sub>2</sub> complex each of the two Ala chelates with the Cu atom, forming a stable five-membered ring where both carboxyl and amino groups are involved. When  $\text{TiO}_2$  is present, one of the two functional groups of Ala, most likely the carboxyl group, chelates with a Ti atom on the nanoparticle surface, resulting in the collapse of the five-membered ring structure. However, in the  $\text{Hg}^{2+}/\text{TLA}$  complex, the sulfhydryl group from three or four TLA molecules is the sole functional group that chelates with  $\text{Hg}^{2+}$ , leaving the carboxyl group free at the other end of the molecule. When  $\text{TiO}_2$  is added, the carboxyl group will chelate with  $\text{TiO}_2$  while retaining the first-shell S atoms around Hg. Although this explanation is completely reasonable

for the observed XAFS spectra, it cannot readily explain the difference in photoreduction enhancement between Ala and TLA in these two systems, because they both should have one functional group attached to the metal and the other functional group to Ti on the nanoparticle surface. The difference in the photoreduction efficiency deserves further explanation and study. Two possible causes are proposed based on the experimental results. First, the affinity of S for Hg may be higher than Cu for N (in  $\text{NH}_2$ ), because the Cu to first-shell atom distance in  $\text{Cu}^{2+}/\text{Ala}/\text{TiO}_2$  is the same as Cu in  $\text{H}_2\text{O}$ , indicating that Cu atoms may be associated with  $\text{H}_2\text{O}$  or carboxyl instead of N atoms of Ala. This higher affinity between the S-containing ligand and the metal ion may affect the reaction efficiency. Second, the possible formation of HgS could reduce the efficiency of photoreduction to  $\text{Hg}^0$ . At this point, our observations imply that a proper balance between the affinities of the metal to the adsorber and surface O atom of  $\text{TiO}_2$  may be one of the keys in selecting a proper surface adsorber for an enhanced photoreduction efficiency of the metal ions on nanoparticle surfaces.

**Acknowledgment.** This work is supported by the Chemical Science Division, Office of Basic Energy Science, U.S. Department of Energy, under Contract W-31-109-Eng-38. We thank Dr. Olga Mićić for her generous help in providing  $\text{TiO}_2$  particles with 30 and 200 Å diameters, Dr. David M. Tiede for his inspiring discussions, and Dr. Farrel Lytle for his  $\text{Hg}^0$  spectra and helpful suggestions. We also appreciate the support from Dr. Pedro A. Montano and the personnel at Beamlines X6B, X18B, and X19A, National Synchrotron Light Source, Brookhaven National Laboratory.

## References and Notes

- (1) *Homogeneous and Heterogeneous Photocatalysis*; Pelizzetti, E., Serpone, N., Eds.; NATO ASI Ser. C **1986**, 174.
- (2) *Photocatalysis—Fundamentals and Applications*; Serpone, N., Pelizzetti, E., Eds.; John Wiley and Sons: New York, 1989.
- (3) Stafford, U.; Gray, K. A.; Kamat, P. V. *Heterog. Chem. Rev.* **1996**, 3, 77.
- (4) Serpone, N. *Res. Chem. Intermed.* **1994**, 20, 953.
- (5) Hoffmann, M. R.; Martin, S. T.; Choi, W. Y.; Bahnemann, D. W. *Chem. Rev.* **1995**, 95, 69.
- (6) Linsebigler, A. L.; Lu, G. Q.; Yates, J. T. *Chem. Rev.* **1995**, 95, 735.
- (7) Serpone, N.; Lawless, D.; Terzian, R.; Minero, C.; Pelizzetti, E. In *Photochemical Conversion and Storage of Solar Energy*; Kluwer Academic Publishers: Dordrecht, The Netherlands, 1991; pp 451–475.
- (8) (a) Foster, N. S.; Noble, R. D.; Koval, C. A. *Environ. Eng.* **1988**, 27, 651. (b) Jacobs, J. W.; Kampers, F. W. H.; Rikken, J. M. G.; Bulle-Lieuwma, C. W. T.; Koningsberger, D. C. *J. Electrochem. Soc.* **1989**, 136, 2914.
- (9) Foster, N. S.; Lancaster, A. N.; Noble, R. D.; Koval, C. A. *Ind. Eng. Chem. Res.* **1995**, 34, 3865.
- (10) Forouzan, F.; Richards, T. C.; Bard, A. J. *J. Phys. Chem.* **1996**, 100, 18123.
- (11) (a) Rajh, T.; Ostafin, A. E.; Micic, O. I.; Tiede, D. M.; Thurnauer, M. C. *J. Phys. Chem.* **1996**, 100, 4538–4545. (b) Rajh, T.; Tiede, D. M.; Thurnauer, M. C. *J. Non-Cryst. Solids* **1996**, 207, 815–820.
- (12) Klabunde, K. J.; Stark, J.; Koper, O.; Mohs, C.; Park, D. G.; Decker, S.; Jiang, Y.; Lagadic, I.; Zhang, D. *J. Phys. Chem.* **1996**, 100, 12142.
- (13) Thurnauer, M. C.; Rajh, T.; Tiede, D. M. *Acta Scand.* **1997**, 51, 5.
- (14) *X-ray Absorption: Principles, Applications, Techniques of EXAFS, SEXAFS, and XANES*; Koningsberger, D. C., Prins, R., Eds.; Wiley: New York, 1988.
- (15) Rajh, T.; Saponjic, Z. V.; Micic, O. I. *Langmuir* **1992**, 8, 1265.
- (16) Bragg, L.; Claringbull, G. F. *Crystal Structures of Minerals*; G. Bell & Sons Ltd.: London, 1965.
- (17) Tomita, K.; Nitta, I. *Bull. Chem. Soc. Jpn.* **1961**, 34, 286.
- (18) Åsbrink, S.; Norrby, L. *J. Acta Crystallogr.* **1970**, B26, 8.
- (19) Aurivillius, K. *Acta Crystallogr.* **1956**, 9, 685.
- (20) Aurivillius, K. *Acta Chem. Scand.* **1964**, 18, 1552.
- (21) Serpone, N.; Lawless, D.; Khairutdinov, R. *J. Phys. Chem.* **1995**, 99, 16646.
- (22) Grunes, L. A. *Phys. Rev. B* **1983**, 27, 2111.

- (23) Greigor, R. B.; Lytle, F. W.; Sandstrom, D. R.; Wong, J.; Schultz, P. *J. Non-Cryst. Solids* **1983**, *55*, 27.
- (24) Pei, S.; Zajac, G. W.; Kaduk, J. A.; Faber, J.; Boyanov, B. I.; Duck, D.; Fazzini, D.; Morrison, T. I.; Yang, D. S. *Catal. Lett.* **1993**, *21*, 333.
- (25) Yamashita, H.; Ichihashi, Y.; Anpo, M.; Hashimoto, M.; Louis, C.; Che, M., *J. Phys. Chem.* **1996**, *100*, 16041.
- (26) Ruiz-López, M. F.; Muñoz-Páez, A. *J. Phys: Condens. Matter* **1991**, *3*, 8981.
- (27) Bohr, F.; Ruiz-López, M. F.; Muñoz-Páez, A. *Catal. Lett.* **1993**, *20*, 59.
- (28) Poumellec, B.; Marucco, J. F.; Touzelin, B. *Phys. Rev. B* **1987**, *35*, 2284.
- (29) Oxtoby, D. W.; Nachtrieb, N. H. *Principles of Modern Chemistry*; Saunders College Publishing: Philadelphia, 1987.
- (30) Miyanaga, T.; Watanabe, I.; Ikeda, S.; Tashiro, K.; Fujikawa, T. *Bull. Chem. Soc. Jpn.* **1988**, *61*, 3199.
- (31) (a) Hasegawa, K.; Neta, P. *J. Phys. Chem.* **1978**, *82*, 859. (b) Tamba, M.; Badiello, R. *Ind. J. Radiat. Biol. Relat. Stud. Phys. Chem. Med.* **1985**, *48*, 259. (c) *Encyclopedia of Electrochemistry of the Elements, Organic Section*; Bard, A. J., Lund, H., Eds.; Marcel Dekker: New York, 1978; Vol. XII, p 269.
- (32) Nogami, G.; Kennedy, J. H. *J. Electrochem. Soc.* **1989**, *136*, 2583.
- (33) Micic, O. I.; Zhang, Y.; Cromack, K. R.; Trifunac, A. D.; Thurnauer, M. C. *J. Phys. Chem.* **1993**, *97*, 13284–13288.
- (34) Kau, L.-S.; Spira-Solomon D. J.; Penner-Hahn, J. E.; Hodgson, K. O.; Solomon, E. I. *J. Am. Chem. Soc.* **1987**, *109*, 6433.
- (35) Wright, J. G.; Tsang, H.-T.; Penner-Hahn, J. E.; O'Halloran, T. V. *J. Am. Chem. Soc.* **1990**, *112*, 2434.